Near unity narrowband infrared thermal emitters on silicon with silicon carbide-germanium metasurfaces ⊕

Patrick Rufangura ⓘ ; Yiyang Cui ⓘ ; Huan Liu; Johan D Carlstrom; Kenneth Crozier ✉ ⓘ ;
Mark L Brongersma ✉ ; Yang Yang ⓘ ; Francesca Iacopi ✉ ⓘ

Check for updates

View Online   Export Citation

Articles You May Be Interested In

Invited Article: Narrowband terahertz bandpass filters employing stacked bilayer metasurface antireflection structures

APL Photonics (February 2018)

Simultaneous single-peak and narrowband thermal emission enabled by hybrid metal-polar dielectric structures

Appl. Phys. Lett. (August 2019)

Narrowband, infrared absorbing metasurface using polystyrene thin films

J. Appl. Phys. (February 2020)
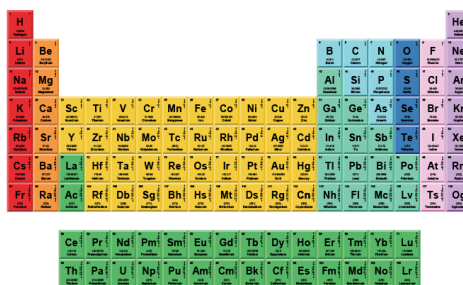
Near unity narrowband infrared thermal emitters on silicon with silicon carbide-germanium metasurfaces 🄴🄿

Patrick Rufangura,[1,2] 🄳 Yiyang Cui,[3] 🄳 Huan Liu,[4] Johan D Carlstrom,[5] Kenneth Crozier,[4,a] 🄳
Mark L Brongersma,[5,a] Yang Yang,[1,2] 🄳 and Francesca Iacopi[1,2,6,a] 🄳

AFFILIATIONS

[1] School of Electrical and Data Engineering, Faculty of Engineering and Information Technology, University of Technology Sydney, Broadway 2007, New South Wales, Australia
[2] Centre of Excellence in Transformative Meta-Optical Systems, University of Technology Sydney, Broadway 2007, New South Wales, Australia
[3] Department of Electrical and Electronic Engineering, University of Melbourne, Melbourne, Victoria 3010, Australia
[4] ARC Centre of Excellence for Transformative Meta-Optical Systems, School of Physics, University of Melbourne, Melbourne 3010, Victoria, Australia
[5] Geballe Laboratory for Advanced Materials, Stanford University, 476 Lomita Mall, Stanford, California 94305, USA
[6] Indiana R&D Centre, Imec USA, 101 Foundry Drive, West Lafayette, Indiana 47906, USA

[a] Authors to whom correspondence should be addressed: kenneth.crozier@unimelb.edu.au; markb29@stanford.edu; and francesca.iacopi@uts.edu.au

ABSTRACT

Traditional thermal emitters are characterized by an incoherent broadband emission spectrum. However, narrowband coherent thermal emission with a high-quality factor in thermally stable materials is highly desirable for applications such as sensing, thermal energy management, thermophotovoltaic systems, and other infrared technologies. Recent advances in engineered nanostructured polaritonic materials, particularly polar dielectric materials in the mid-infrared (MIR) regime, have enabled new approaches to tailoring narrowband coherent thermal emission. The use of low-loss phonon polaritons in thermally stable silicon carbide provides a promising route to MIR thermal emission. In this work, we demonstrate narrowband, near-unity MIR thermal emission by coupling coherent surface phonon polaritons in a SiC layer with a subwavelength germanium grating on a silicon substrate. The demonstrated polarization-dependent thermal emitter, compatible with silicon fabrication technologies for seamless on-chip photonic integration, exhibits narrowband high emissivity (>90%) at a wavelength of ~11 μm. Furthermore, we show that these emitters achieve experimental quality factors well above 100 while maintaining significant emission across a wide range of incident angles for MIR radiation.

I. INTRODUCTION

The fundamental principles of statistical mechanics state that every absorbing hot object emits electromagnetic waves. According to Planck's law for blackbody radiation, objects at room temperature naturally display thermal emission in the mid-infrared (MIR) region. The peak wavelength (λ_{peak}) at which the emission from a blackbody is maximum is dictated by Wien's law $\lambda_{peak} = \frac{b}{T}$ (where

b = 2898 μm K, which stands for Wien's displacement constant, and T is the absolute temperature in Kelvin). This wavelength is typically in the range of ~9.72–9.89 μm.[1] The concept of thermal radiation has been fundamental for applications such as thermal imaging,[2] incandescent light sources,[3] thermophotovoltaics,[4] thermal camouflage[5,6] and more recently for radiative cooling[7] and many other technologies.[8] There is significant interest in mid-infrared (MIR) thermal emitters, as it is within this spectral region that several gases,

liquids, and solids exhibit vibrational absorption fingerprints.[9,10] Kirchhoff's law of thermal radiation states that at thermal equilibrium, the emissivity, $\xi(\theta, \omega, T)$, of a body is equal to its absorptivity, $A(\theta, \omega, T)$.[5,11] Conventional emitters are typically bulky and generate broadband, unpolarized, and incoherent thermal emission, which limits their use for some applications, such as non-dispersive gas sensing.[12] Engineered subwavelength micro/nanostructures, also known as metasurfaces, enable flexible control of thermal emission properties such as polarization, coherence, quality (Q) factor, and directionality. By carefully tailoring these metasurfaces to manipulate near-field interactions, the control of far-field electromagnetic waves can be significantly enhanced.[13] Thermal emissions with engineered properties have recently gained significant attention due to their ability to offer both fundamental advantages, such as high spatial and temporal coherence, and improved energy efficiency for various practical applications.[14] Among the metasurface-based thermal emitters, micro/nanostructures made of polaritonic materials exhibit many interesting thermal emission characteristics in the MIR spectrum.[5] Surface phonon polaritons (SPhPs), which result from the coupling of the electromagnetic (EM) field of incident light and coherent oscillations of charged atomic species in polar materials, have attracted considerable attention. SPhPs can only be supported in a material-dependent spectral region, known as the Reststrahlen spectral window, bound between longitudinal optical (LO) and transverse optical (TO) frequencies in the MIR spectrum, where polar materials exhibit a negative real part of permittivity. SiC is one such polar material that supports SPhP modes.[15,16] Low intrinsic losses associated with the small scattering rates of the optical phonons in SiC enable the realization of sharp optical resonances with high quality (Q) factors in SiC-based metasurfaces.[15] Greffet et al., reported the first demonstration of MIR coherent thermal emission based on SPhP from patterned SiC microstructures.[17] Subsequently, Arnold et al. reported near-unity coherent thermal emission based on SPhP modes in 2D SiC gratings for both s- and p-polarized MIR radiation.[18] Schuller et al. demonstrated the possibility to create optical antenna thermal emitters that employ Mie resonances to engineer the spectral and polarization-dependent properties of the thermal emission.[19] Wang et al. used SiC-based bowtie nanoantennas to demonstrate narrowband, polarized thermal emission enabled by strong localization of SPhP on the SiC nanoantennas. They also showed control of the emission frequency by adjusting the antenna's feedgap.[13] More recently, Lu et al. used SiC-based nanophotonic IR emitting metamaterials(NIREM) to demonstrate a proof of concept of narrowband polaritonic thermal emitters with low power consumption driven by waste heat in the MIR spectrum regime.[1] Furthermore, MIR thermal emitters were realized in 4H–SiC nanopillars[20] with spectral and spatial coherent thermal emission originating from strong coupling between propagating and localized SPhP and with zone-folded LO phonons, while near-field based thermal emission of localized SPhP were realized in 6H–SiC nanopillars.[21] Although SiC-based polaritonic thermal emitters have demonstrated extraordinary emission properties such as near unity, coherent, and diffuse emissivity, achieving near-unity emissivity in all the reported SiC-based thermal emitters requires metasurfaces of at least 1 μm thickness.[22] It is worth noting that etching SiC is a non-trivial process due to its hardness, which is comparable to that of diamond.[23] Coupling SiC with high refractive index (n) metasurfaces, such as Ge (with an n of ~4.002 and a

low loss of 2 dB cm^{-1} in the MIR region[24]), presents an alternative approach to SiC-only structures to harnessing the unique thermal emission properties of polar dielectric materials in the MIR spectrum. In this approach, Ge-based metasurfaces on SiC films facilitate the excitation of phonon polaritons in SiC,[25] thereby enhancing the absorption and thermal emission in these structures. Qiang et al. demonstrated absorption enhancement of SPhPs using subwavelength germanium (Ge) microdiscs with a thickness of 120 nm and a diameter of 1 μm, patterned on bulk 6H–SiC. This enhancement was shown by near-zero reflection at a wavelength of 11 μm.[26] Subsequently, Cui and Zheng employed 600-nm-thick Ge gratings on a SiC substrate, achieving polarization-sensitive, perfect absorption in the MIR at a wavelength of 11.2 μm.[27] More recently, Ma et al. reported narrowband thermal emission with a high-quality factor (Q factor) of 101 using 80-nm-thick Ge grating coupled to SPhP mode in SiC.[28] Their phonon-mediated Ge nanostructure exhibited spectral coherence in the emitted radiation and strong diffuse thermal emission, with a full angular width at half maximum (FWHM) of 70°.

While there have been recent advancements in phonon-mediated germanium (Ge) structures for MIR thermal emission, all reported designs rely on bulk 4H–SiC and 6H–SiC, which hinder the miniaturization of the final device. Furthermore, the Ge/SiC metasurfaces reported to date exhibit limited Q factors, with the highest reported Q factor being 101.[26] On the other hand, using 3C–SiC films epitaxially grown on silicon wafers,[29,30] metasurfaces with Q factors up to 170 and featuring angularly insensitive emissivity were realized.[22] In addition, this platform enables easy on-chip integration of the device thanks to advanced silicon technologies and allows for better decoupling between adjacent SiC metasurfaces.[31] However, achieving unity emissivity with 3C–SiC still requires thick micro/nanostructures (~1 μm), and the combination of high-index dielectric Ge metasurfaces with thin 3C–SiC films has not been explored in the literature. Therefore, there is a clear need to investigate the emission properties of Ge metasurfaces on 3C–SiC/Si.

In this work, we combine experimental measurements with electromagnetic (EM) simulations based on the Finite Element Method (FEM) to demonstrate the enhancement of MIR thermal emission from 3C–SiC surface phonon polaritons coupled to Ge gratings on a silicon substrate. The Ge gratings/3C–SiC film epitaxially grown on silicon exhibit polarization-sensitive, diffuse, near-unity absorption/thermal emission, exceeding 95%. The simulated and measured Q factors are 232 and 123, respectively, surpassing the highest reported Q factor of 100 for Ge metasurfaces on bulk SiC-based thermal emitters.[26,28] FEM simulation results and infrared (IR) characterization of the fabricated metasurface reveal that the absorption/emission resonance can be tuned by adjusting the thickness of the Ge gratings.

II. RESULTS AND DISCUSSION

To demonstrate narrow absorption and thermal emission based on SPhPs, subwavelength Ge gratings ($< \frac{\lambda_{resonance}}{119}$) on an epitaxial film of 3C–SiC on a Si substrate were designed. Figures 1(a) and 1(b) present a schematic of the finite element method (FEM) model and a scanning electron microscope (SEM) image of the fabricated Ge grating/3C–SiC/Si device. The period, thickness, and width of the
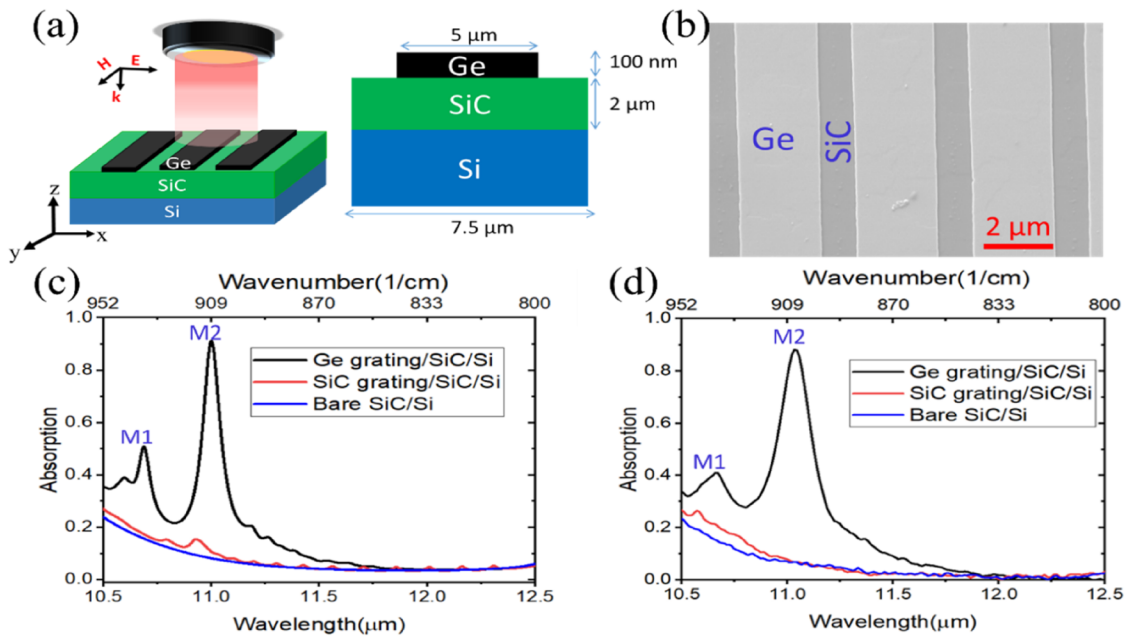
FIG. 1. (a) Schematic of the simulated Ge grating/SiC/Si model, showing both full and cross-sectional views. (b) Scanning electron microscope (SEM) image of the fabricated Ge gratings on SiC/Si. (c) Simulation results for the absorption spectrum, highlighting M1 at 10.6 μm and M2 at 11 μm. (d) Experimental absorption spectrum shows M1 at 10.6 μm and M2 at 11 μm.
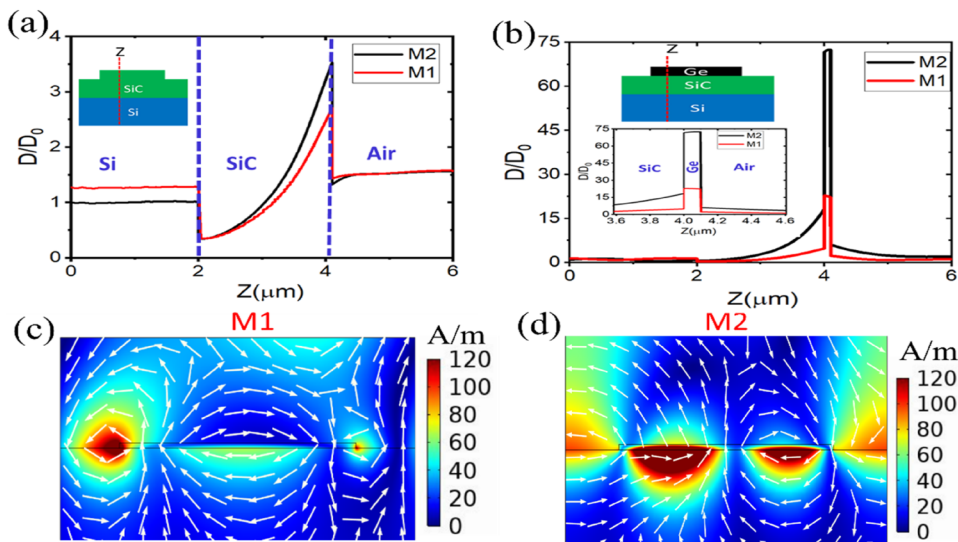

FIG. 2. (a) Calculated electric displacement field enhancement for mode M1 at 10.8 μm and mode M2 at 10.9 μm for the bare SiC grating/SiC/Si structure. The inset shows a schematic of the model with the line (Z) along which the fields are calculated. (b) Calculated electric displacement field (D/D$_0$) enhancement for mode M1 at 10.6 μm and mode M2 at 11 μm for the Ge grating/SiC/Si structure. (c) Simulated magnitude of magnetic field vector profile for mode M1 at 10.6 μm. (d) Simulated magnitude of the magnetic field vector for mode M2 at 11 μm. White arrows in (c) and (d) represent the direction of the electric field vector (E).

gratings are 7.5 μm, 100 nm, and 5 μm, respectively. Details of the simulation methodology and model setup are provided in the experimental section. The Reststrahlen spectrum window for 3C–SiC, within which the SPhP mode can be supported, is bounded between 10.5 and 12.5 μm. Therefore, our study focuses on this spectral range. As expected, unpatterned bare SiC exhibits weak, spectrally flat absorption due to its high reflectivity within the investigated spectral range, coupled with an inability to excite the SPhP mode

with plane wave illumination. This is due to the significant wavevector mismatch between the incident light and the surface phonons in the unpatterned structure.[32] In contrast, simulations of an ultrathin SiC grating (100 nm height) on a SiC/Si substrate reveal two weak absorption (~15%) peaks at wavelengths of 10.7 and 10.8 μm, indicative of weakly excited SPhP modes in the SiC material. For the Ge gratings (100 nm height) coupled to the SiC/Si substrate, both simulations [Fig. 1(c)] and experimental data [Fig. 1(d)] reveal

two prominent narrowband absorption peaks with a Q factor of ~232. The first peak (M1) occurs at 10.6 μm with ~50% absorption, while the second peak (M2) occurs at 11 μm with over 90% absorption.

The significant difference in absorption efficiency between the bare SiC grating on SiC/Si and the Ge grating on SiC/Si can be attributed to the distinct mechanisms underlying the resonances in SiC with and without the Ge grating. These mechanisms are explored by analyzing the optical modes that can be excited under top illumination with the electric field polarized normal to the Ge strips. To analyze which modes are excited, we plot the electric field displacement "D" in the z-direction. This component is continuous through the various horizontal interfaces, that is, $\vec{D_z} = \varepsilon_{Si}\vec{E_{Si}} = \varepsilon_{SiC}\vec{E_{SiC}} = \varepsilon_{Ge}\vec{E_{Ge}} = \varepsilon_{Air}\vec{E_{Air}}$. To analyze the field enhancement, we simulated the electric displacement field along the vertical cutline [red dots line in the inset of Figs. 2(a) and 2(b)] with and without the Ge grating on SiC/Si in the model (denoted as D and D_0, respectively). The electric displacement field enhancement was then calculated as D/D_0 for the SiC grating at M1 = 10.8 μm and M2 = 10.9 μm [Fig. 2(a)] and the Ge grating/SiC at M1 = 10.6 μm and M2 = 11 μm [Fig. 2(b)]. Conceptually, each SiC grating can be viewed as an array of cavities that support surface phonon polariton (SPhP) modes.[26,27] However, the 100-nm-thick SiC grating is significantly smaller than the decay length of the evanescent wave supported by the SiC–air interface. As a result, the edges of the grating strips introduce minor perturbations to the polaritonic fields, leading to inefficient coupling of the incident photons with the surface optical phonons in SiC, resulting in weak coupling into the SPhP mode. This effect is also evidenced by the fact that the simulated electric displacement field enhancement is

only 3.5 at the interface between the shallow SiC grating and the air interface, as depicted in Fig. 2(a). This inefficient confinement of the polaritonic field in the shallow SiC grating/SiC/Si structure leads to negligible absorption, as shown in Figs. 1(c) and 1(d). Previous literature has shown that achieving strong SPhP mode resonance and high absorption in SiC requires deep dry etching of SiC microstructures to ~1 μm in height.[20,22,33,34] In contrast, the combination of a Ge grating with a flat SiC substrate forms composite resonant cavities that support ultra-confined surface phonon polariton waves,[25,35] which significantly reduce the decay length of the polaritonic (evanescent) wave at the SiC–Ge interface and enable critical coupling between incident EM fields with the polaritonic fields, leading to efficient confinement of the fields in the Ge grating/SiC/Si device. As shown in Fig. 2(b), the field analysis of the Ge grating/SiC/Si structure demonstrates a strong enhancement of the electric displacement field by a factor of 75 within the Ge, indicating deep subwavelength confinement of the mid-infrared (MIR) fields (λ_0 = 11 μm) within the 100 nm Ge grating. This results in significant absorption enhancement in the Ge grating/SiC/Si model, as observed in Figs. 1(c) and 1(d).

To understand the absorption characteristics of the Ge grating/SiC/Si device, we analyzed the magnitude of the magnetic field vector profiles for both modes, M1 and M2, as shown in Figs. 2(c) and 2(d). For mode M1, the magnetic field exhibits the strongest enhancement at the left edge of the grating, with weaker enhancements at the right edge and the Ge-SiC interface. This behavior suggests that M1 is primarily driven by Ge grating coupling to a dispersive SiC surface polariton mode and thus highly sensitive to the angle of the incident light, with the mode disappearing under normal
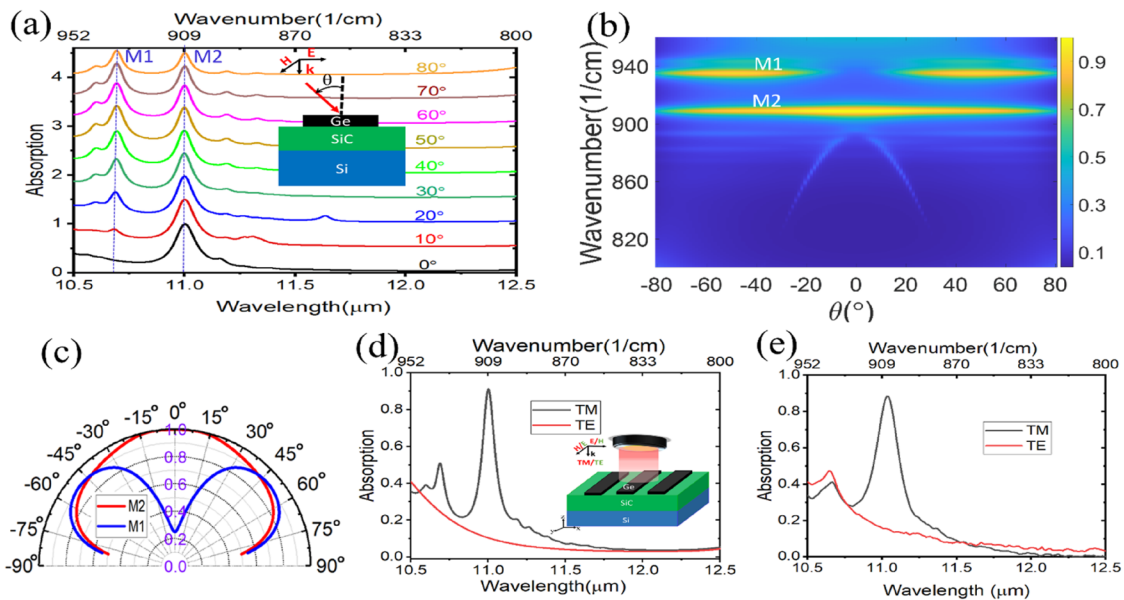
FIG. 3. (a) Simulated angular-dependent absorption. (b) Absorption map for different angles and directions of incident radiation of the Ge gratings/SiC/Si. (c) Polar plot showing simulated angular peak absorption for M1 and M2. (d) Simulated and (e) measured absorption spectra of the Ge grating/SiC/Si for TE and TM polarization, respectively.

incidence. In contrast, the magnetic field profile for mode M2 shows the strongest confinement at the Ge-SiC interface. The variation in the magnitude of the displacement current indicates the excitation of the lowest order resonance for mode M1 with approximately half a SPhP wave fitting across the width of the strip and a full-standing wave nature for mode M2 [see white arrows in Figs. 2(c) and 2(d)].

To investigate spatial control of the Ge grating/SiC/Si-based thermal emitters, simulations are performed of the dependence of absorption/emissivity on the angle of incident radiation θ. Here we keep the p-polarized illumination, and the grooves of the grating are perpendicular to the plane of incidence, varying the incident angle θ from 0° (normal incidence) to 80°. The simulated angle-dependent absorption spectra are presented in Fig. 3(a). At θ = 0°, only the fundamental mode M2 is excited due to the matching of the incident light's wave vector with that of the surface phonon in SiC, resulting in the strongest coupling and near-unity absorption in the Ge grating/SiC/Si structure. As the angle of incidence increases (θ ≥ 10°), an additional mode, M1, emerges, with its absorption enhancing as θ increases, reaching 92% at θ = 40°. High absorption, exceeding 80%, is maintained for both M1 and M2 over a broad range of incident angles up to θ = 60°, and it gradually decreases to ~50% at θ = 80°. These results indicate that the investigated device can support thermal emission over a broad range of angles. As shown in Figs. 3(b) and 3(c), the simulated absorption spectra

reveal that the resonance wavelengths for M1 and M2 are independent of the direction of the incident radiation, as evidenced by the absorption map and polar plot for both negative and positive incident angles. This suggests that the fabricated Ge grating/SiC/Si metasurface is capable of generating temporally coherent thermal emission.[17,36] Furthermore, the polarization dependence of absorption in the metasurfaces is examined. Figures 3(d) and 3(e) present the simulated and measured absorption for TM and transverse electric (TE) polarized sources, respectively. Both the simulation and measurement show peak absorption for modes M1 and M2 under TM polarization, while the absorption becomes spectrally flat under TE polarization. This demonstrates that the device is highly sensitive to the polarization of the incident light source.

We next investigate the dependence of the metasurface resonances on the thickness of the Ge grating. The grating thickness was varied from 100 to 200 nm while other geometric parameters remained fixed. Figure 4 shows both simulated and experimentally measured absorption spectra for different Ge thicknesses (H). The simulation results [Figs. 4(a) and 4(b)] show nearly perfect absorption (99%) for H = 120 nm, which is confirmed by the measured absorption of ~96% for the same thickness [Fig. 4(c)]. Strong absorption in the infrared spectral region is crucial for various practical applications, such as thermal cooling,[30] thermal energy[37] management,[38] and gas sensing.[39–41] Furthermore, both simulation and experimental results demonstrate that the resonant wavelength of
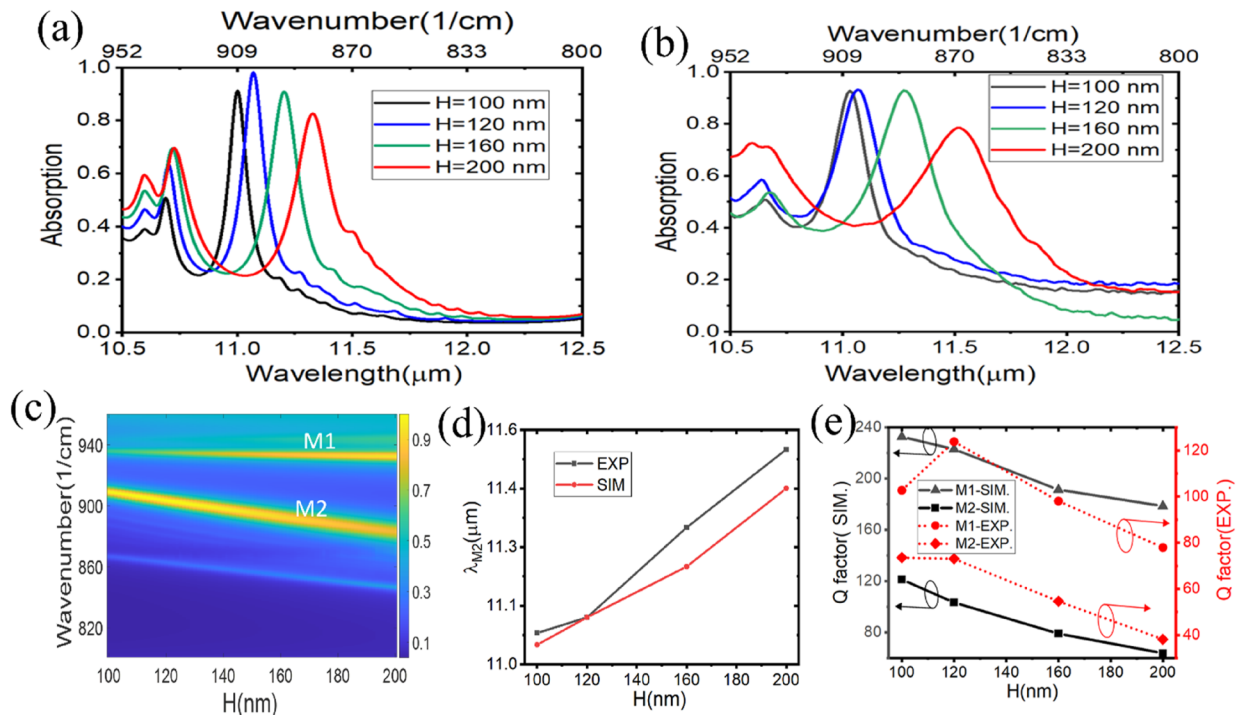
FIG. 4. Absorption characteristics of the Ge gratings/SiC/Si with different grating thicknesses (H): (a) Simulated absorption spectra for various Ge grating thicknesses. (b) Measured absorption spectra for different Ge grating thicknesses. (c) Simulated absorption map showing the angular and spectral dependence of various absorption features. (d) Simulated and measured resonance wavelengths of mode M2 for varying Ge grating thicknesses, demonstrating the tunability of the device. (e) Simulated and measured Q factors for M1 and M2 for varying grating thickness H.

mode M2 experiences a redshift of up to 400 nm as the grating thickness increases from 100 to 200 nm, indicating the tunable (static) nature of the Ge gratings/SiC/Si device [Fig. 4(d)]. In addition, an analysis of the quality factors for both measured and simulated absorption/emission [Fig. 4(e)], reveals high theoretical and experimental Q factors: 232 and 123 for M1, and 121.3 and 73.5 for M2, respectively. These values are higher than those reported for most plasmonic[42,43] and phononic-based metasurfaces.[15,28,44] As shown in Fig. 4(e), the Q factors tend to decrease with increasing grating thickness, with the highest theoretical Q achieved for a 100 nm Ge grating. We attribute this trend to material losses in the grating: although Germanium exhibits relatively low absorption in the MIR spectrum, it still introduces some loss. A shallower Ge grating confines most of the surface phonon polariton (SPhP) field to the SiC–air interface, where material losses are minimal, resulting in a higher Q factor. In contrast, a thicker Ge grating increases the mode overlap with the Ge material itself, leading to greater absorptive losses, broader linewidths, and thus lower Q factors. The slight discrepancy between the simulated and measured Q factors can be attributed to fabrication and measurement imperfections.

Furthermore, we investigate the effect of the grating width (W) and gap (G) by simulating the model at different grating filling fractions ($FF = \frac{W}{W+G}$). The simulation results for varying FF values, with a constant period of 7.5 μm, are presented in Figs. 5(a) and 5(b). These results demonstrate a strong dependence of absorption on

the filling fraction of the Ge grating/SiC/Si device. For mode M1, absorption remains strong at small FF values (corresponding to a larger grating gap) and decreases significantly for FF values greater than 0.7. As previously discussed, M1 is excited by obliquely incident light. Therefore, a wider grating gap facilitates increased radiation interaction with the grating edge, leading to strong coupling efficiency and high absorption. Magnetic field analysis along the grating strip revealed a half-standing wave nature for mode M1 [Fig. 2(c)], indicating that strong confinement and absorption require a wider gap and smaller grating width. In contrast, mode M2 exhibits strong absorption at larger filling fractions (i.e., wider grating widths, W), as shown by the simulated near 100% absorption for FF = 0.9. This behavior is further supported by the field analysis for M2, which indicated a full-standing wave nature for this mode [Fig. 2(d)]. In addition, it is observed that the resonant wavelength of mode M2 experiences a blue shift as the FF value increases. We also explored the effect of the grating period, Λ, on the absorption behavior of the proposed device by varying the grating period from 1 to 10 μm while maintaining a constant filling fraction of FF = 0.67. The simulated absorption spectra for different grating periods are shown in Fig. 5(c). As the grating period increases, the absorption spectrum of mode M1 exhibits a redshift and becomes broader, eventually almost becoming flat for Λ = 6 μm. After this point, the absorption begins to increase and reaches a high value for Λ = 10 μm. In contrast, the absorption spectrum for mode M2 exhibits a blueshift as Λ increases from 1 to 5 μm, and a redshift for all $\Lambda \geq 6$ μm, accompanied by a
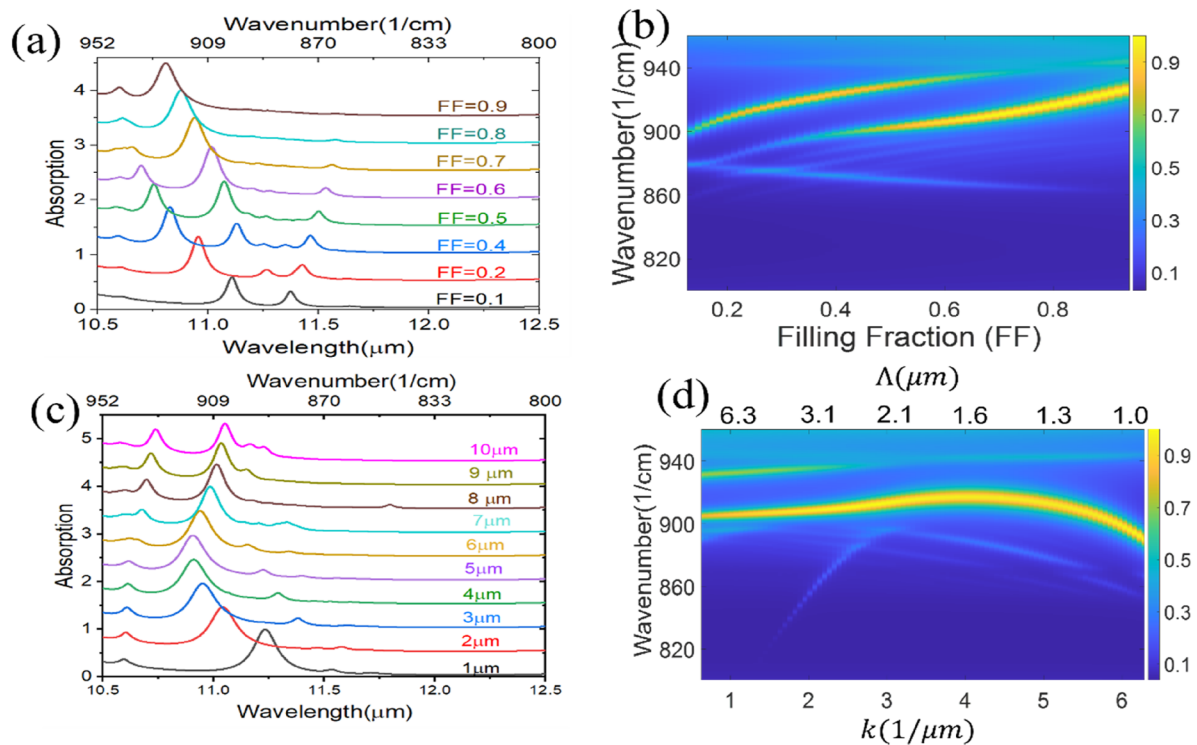

FIG. 5. Absorption characteristics of the Ge grating/SiC/Si for different values of grating filling fraction (FF): (a) absorption spectra, (b) absorption map for different FF values, (c) absorption spectra for different grating period, and (d) absorption map for the different grating periods plotted vs their corresponding k vector ($k = \frac{2\pi}{\Lambda}$).
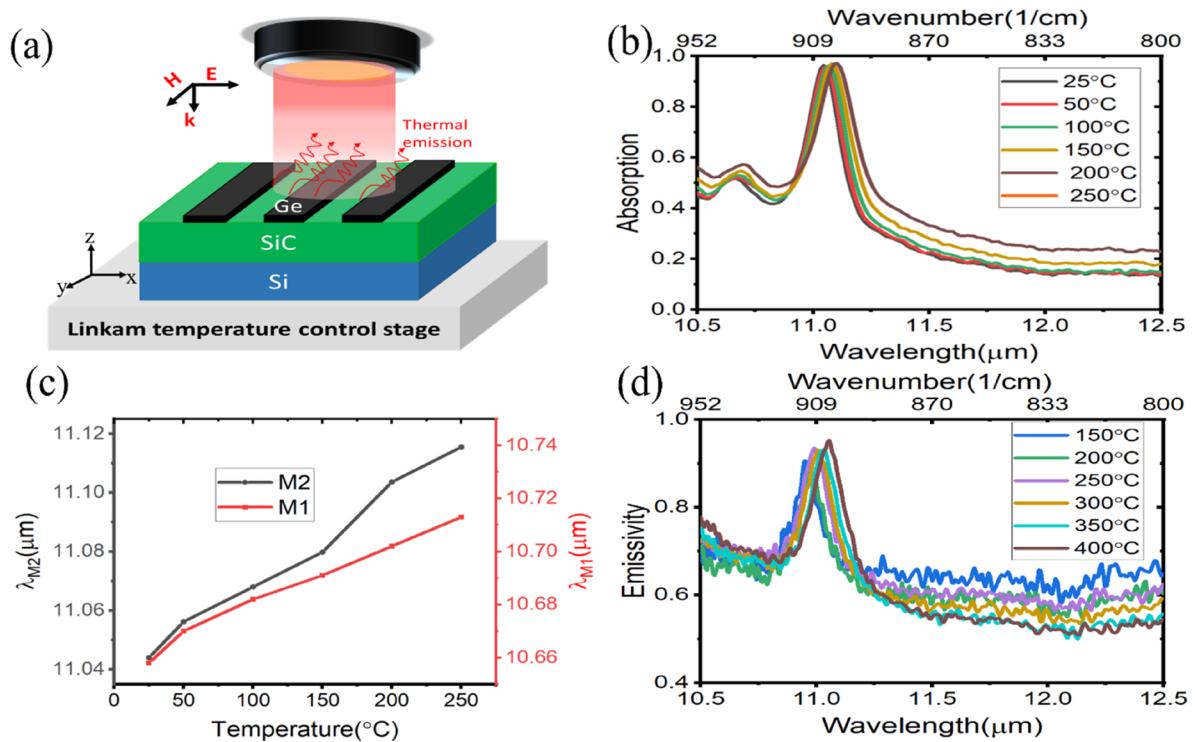
FIG. 6. (a) Schematic of the Ge grating/SiC/Si device with the heating stage for temperature-dependent absorption and emissivity measurements. (b) Absorption spectra measured at different temperatures. (c) Peak resonance wavelengths for modes M1 and M2 at varying temperatures. (d) Measured emissivity of the fabricated device at different temperatures.

decrease in absorption. This behavior can be described by anomalous dispersion ($k = 2\pi/\Lambda$), along with the absorption spectral map for different Ge grating periods as shown in Fig. 5(d).

To investigate the thermal behavior of the device, temperature-dependent absorption measurements are performed on the fabricated Ge gratings/3C–SiC/Si using a temperature control stage unit [Fig. 6(a)]. The absorption dependence on temperature was recorded by heating the sample from 25 to 250 °C. As shown in Fig. 6(b), a noticeable slight increase in absorptivity is observed as the temperature rises. In addition, a redshift of the resonant peaks is observed with increasing temperature [Fig. 6(c)]. This shift is attributed to the temperature-induced increase in the refractive index of SiC.[28,36] Finally, the thermal emissivity characteristics of the fabricated metasurface were tested by measuring the emissions from the device at various temperatures. As expected, a satisfactory correlation is observed between the measured emissivity of the fabricated samples and the temperature-dependent absorption of the emitter, satisfying Kirchhoff's law of thermal radiation.[5,11] The measurements revealed an emissivity enhancement of more than 5%, increasing from 90% to ~95% as the sample's temperature rose from 150 to 400 °C [Fig. 6(d)]. Moreover, the observed emissivity enhancement dependence on the increasing temperature of the sample indicates the spectral coherence nature of emission in the fabricated Ge gratings/SiC/Si thermal emitters, mediated by

excitation of surface phonon polaritons on the surface of SiC, as reported in Ref. 45 for polariton-based coherent thermal emission.

Finally, we analyzed the relationship between the Q factor and the spatial extent of the resonant modes. For the highest theoretical Q of 232 at 11 μm, we estimate a mode lifetime ($\tau = \frac{Q}{\omega}$) of ~1.3 ps and a group velocity (v_g) of 1.5×10^7 m/s, yielding a lateral propagation length ($L_P = \tau \times v_g$) of 20 μm. This exceeds the free-space wavelength (~11 μm), indicating that thermally excited SPhP modes in the Ge/SiC metasurface can propagate over tens of micrometers. Such nonlocal behavior implies that neighboring features may couple or interfere, enabling complex functionalities for applications in thermal imaging, near-field energy transport, infrared communication, and reconfigurable metasurfaces.

III. CONCLUSION

In summary, we have theoretically and experimentally demonstrated near-unity, narrowband, polarized thermal emission in subwavelength germanium gratings coupled to 3C–SiC phonon polaritons on a silicon substrate. The demonstrated Ge grating/SiC/Si device exhibits high emissivity, exceeding 95%, with the highest theoretical and experimental quality factors of 232 and 123, respectively, surpassing most existing polar and plasmonic material-based MIR thermal emitters reported in the literature. We show

that polarization-sensitive narrowband thermal emission remains as high as 80% across a broad range of incident angles, owing to the diffuse nature of the thermal emission in the Ge gratings/SiC/Si metasurfaces. In addition, the emission wavelength can be statically tuned up to 400 nm above the resonant wavelength by adjusting the thickness of the germanium grating within a range of 100–200 nm. Temperature-dependent measurements of the fabricated metasurfaces reveal high and spectrally coherent MIR emissions as the sample temperature increases up to 400 °C. We anticipate that the fabricated subwavelength Ge gratings/SiC/Si device, with its compatibility with silicon fabrication technologies for seamless on-chip integration, will be well-suited for a variety of MIR applications, including environmental monitoring sensors, thermal camouflage, and thermal radiation management, among others.

IV. MATERIALS AND METHODS

A. Metasurfaces fabrications

The lithography fabrication flowchart of the Ge gratings/SiC/Si is shown in Fig. 7. 3C–SiC films of 2 μm thickness, epitaxially grown on silicon wafers, were purchased from NOVASiC in France. The wafer was diced into 1×1 cm^2 small chips. The diced samples were submerged in acetone for 3 min followed by immersion in isopropyl alcohol (IPA) for 1 min, and then dried with dry air for cleaning. A layer of Ge films (100 nm) was deposited on the SiC samples using an electron beam thermal evaporator (AJA ATC-1800-E) at a deposition rate of 1 Å/s. The samples were then spin-coated with AZ 1512 HS photoresist at 4000 rpm and baked on a hot plate at 110 °C for 1 min.

Next, photolithography was performed using a maskless aligner (Heidelberg MLA 100) to write the pattern on the samples, followed by development using AZ 726 MIF developer for 45 s and immersion in deionized (DI) water for 1 min. Afterward, Ge gratings were created via reactive ion etching (RIE) using a Plasma-Therm Vision 320 system with a mixed gas recipe on a silicon handling wafer. The etch parameters were RF power = 125 W, chamber pressure = 15 mTorr, process temperature = 20 °C, and gas flow rates of SF$_6$/CF$_4$/CHF$_3$/O$_2$ = 2/45/4/1.5 sccm, respectively. The samples were etched for 85 s, resulting in 100-nm-thick Ge gratings on 3C–SiC/Si.

B. IR characterizations

1. Room temperature absorption measurement

The room temperature reflection spectra for Ge gratings/3C–SiC/Si were collected using a Nicolet Continuμm IR microscope connected to a Thermo Scientific FTIR spectrometer, equipped with a HgCdTe (MCT) detector cooled by liquid nitrogen. The FTIR microscope is fitted with a 15× Infinity Reflachromat objective with a numerical aperture (NA) of 0.58, which illuminates the samples with a half-cone incident angle varying between 0° and 35°. A polarizer (PIKE Technologies) was used to measure the polarization dependence of the reflection spectra. A gold mirror was used as the reference sample, and the absorption spectrum was calculated from the measured reflection using the formula A = 1 − R. It is worth noting that within the investigated spectral range—the Reststrahlen band—SiC behaves as an optically opaque material, characterized by high reflectivity and modest absorptance arising from strong phonon-polariton resonances;[15,46,47] hence, the transmission (T) from the Ge gratings/SiC/Si device is assumed to be negligible.

2. Temperature-dependent absorption measurements

For the temperature-dependent reflection/absorption measurements, a temperature-controlled heating system (Linkam stage) was integrated into the FTIR microscope setup. The sample was mounted on a hot Linkam stage and allowed to stabilize for 5 min before collecting the spectra to ensure temperature equilibration. The reflection spectra were collected using the 15× Cassegrain objective, and absorption spectra were calculated from the measured reflection.

3. Emission measurements

Thermal emission from the fabricated sample was measured with a PerkinElmer Fourier transform Infrared (FTIR) spectrometer. The sample was placed on the Linkam stage, which is vertically oriented and directed toward the external port of the FTIR. The fused silica window of the Linkam stage was removed to prevent IR absorption. The sample was heated to elevated temperatures ranging from 150 to 400 °C, acting as the external IR source for the FTIR. The emission from the sample was collected and guided through a KBr
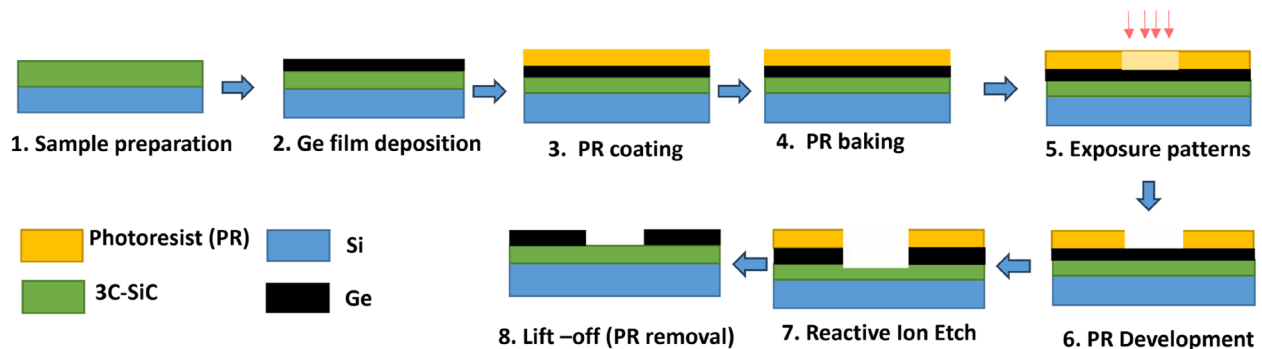
FIG. 7. Lithography fabrication flowchart of germanium gratings on 3C–SiC on Si.

window into the FTIR's internal beam path. An aperture was used to limit the emitting area of the sample. After passing through the interferometer, the signal was measured by a liquid nitrogen (LN) cooled mercury-cadmium-telluride (MCT) detector (IR Associates Inc.). A blackened tungsten (W) film (a 400 nm W film sputtered on a 10×10 mm^2 Si substrate, then blackened with candle soot) was used as the blackbody reference. We measured the emission from the blackbody reference using the FTIR setup at the same temperature as the sample. The emissivity was then obtained by the ratio of the emission from the sample $\left[I_{sample}(T, \omega) \right]$ to the emission measured from the blackbody reference $[I_{blackbody}(T, \omega)]$, Emissivity, $\epsilon(T, \omega) = \frac{I_{sample}(T, \omega)}{I_{blackbody}(T, \omega)}$.

C. Numerical simulations

Full-wave electromagnetic simulations were performed using the finite element method (FEM) with the RF module (electromagnetic waves, frequency domain) in COMSOL Multiphysics 6.2. The unit cell geometry and parameters of the simulated model are defined in the text and shown in Fig. 1(a). Periodic boundary conditions were applied in the x and y directions to mimic the fabricated arrays of Ge grating/SiC/Si. Unless stated otherwise, for all simulations, the model was excited with a TM/p-polarized wave, with the electric field perpendicular to the grating strips. The frequency-dependent permittivity measured for our 3C–SiC membrane was used as input for the dielectric function of SiC[48] and can also be reproduced using a Lorentz oscillator/TOLO formalism:[49,50]

$$\varepsilon(\omega) = \varepsilon_\infty \left(1 + \frac{\omega_{Lo}^2 - \omega_{To}^2}{\omega_{To}^2 - \omega^2 - i\gamma\omega} \right),$$

where ε_∞ represents the high-frequency permittivity while, ω_{TO} and ω_{LO} symbolize the TO and LO phonon frequencies correspondingly, and γ describes the damping constant associated with the optic phonon mode. With $\omega_{TO} = 797$ cm^{-1} and $\omega_{LO} = 973$ cm^{-1}, $\varepsilon_\infty = 6.52$, and $\gamma = 12$ cm^{-1} were used as fit parameters in the equation. Absorption was calculated from reflection using A = 1−R. The simulations used real, lossless permittivity values: 16.2 for germanium and 11.7 for silicon.[51] To match the simulated results with the measurements, the reflection spectrum was simulated by varying the incident angles from 0° to 35°, with the final spectrum being the average of these results.

AUTHOR DECLARATIONS

Conflict of Interest

The authors have no conflicts to disclose.

Author Contributions

Patrick Rufangura: Conceptualization (equal); Data curation (lead); Formal analysis (equal); Methodology (equal); Visualization (lead); Writing – original draft (lead). **Yiyang Cui**: Data curation (supporting); Formal analysis (supporting); Investigation (supporting); Visualization (equal). **Huan Liu**: Data curation (equal); Formal analysis (equal); Investigation (supporting); Visualization (supporting). **Johan D Carlstrom**: Data curation (supporting); Formal analysis (supporting); Investigation (supporting); Visualization (supporting). **Kenneth Crozier**: Conceptualization (supporting); Formal analysis (supporting); Funding acquisition (equal); Methodology (supporting); Supervision (supporting); Writing – review & editing (equal). **Mark L Brongersma**: Conceptualization (equal); Formal analysis (equal); Funding acquisition (supporting); Methodology (equal); Supervision (supporting); Writing – review & editing (equal). **Yang Yang**: Investigation (supporting); Project administration (supporting); Resources (supporting); Supervision (supporting); Writing – review & editing (supporting). **Francesca Iacopi**: Conceptualization (equal); Formal analysis (equal); Funding acquisition (equal); Investigation (equal); Methodology (equal); Project administration (lead); Resources (lead); Supervision (lead); Writing – review & editing (equal).

DATA AVAILABILITY

The data that support the findings of this study are available from the corresponding authors upon reasonable request.

REFERENCES

[1] G. Lu *et al.*, "Narrowband polaritonic thermal emitters driven by waste heat," ACS Omega **5**, 10900–10908 (2020).

[2] M. Vollmer, in *Computer Vision: A Reference Guide 1-4* (Springer, 2020).

[3] O. Ilic *et al.*, "Tailoring high-temperature radiation and the resurrection of the incandescent source," Nat. Nanotechnol. **11**, 320–324 (2016).

[4] C.-C. Chang *et al.*, "High-temperature refractory metasurfaces for solar thermophotovoltaic energy harvesting," Nano Lett. **18**, 7665–7673 (2018).

[5] D. G. Baranov *et al.*, "Nanophotonic engineering of far-field thermal emitters," Nat. Mater. **18**, 920–930 (2019).

[6] O. Salihoglu *et al.*, "Graphene-based adaptive thermal camouflage," Nano Lett. **18**, 4541–4548 (2018).

[7] M. Lee *et al.*, "Photonic structures in radiative cooling," Light: Sci. Appl. **12**, 134 (2023).

[8] J. E. Vázquez-Lozano and I. Liberal, "Review on the scientific and technological breakthroughs in thermal emission engineering," ACS Appl. Opt. Mater. **2**, 898–927 (2024).

[9] M. Vainio and L. Halonen, "Mid-infrared optical parametric oscillators and frequency combs for molecular spectroscopy," Phys. Chem. Chem. Phys. **18**, 4266–4294 (2016).

[10] H. Hu *et al.*, "Far-field nanoscale infrared spectroscopy of vibrational fingerprints of molecules with graphene plasmons," Nat. Commun. **7**, 12334 (2016).

[11] G. Kirchhoff, "I. On the relation between the radiating and absorbing powers of different bodies for light and heat," London, Edinburgh Dublin Philos. Mag. J. Sci. **20**(130), 1 (1860).

[12] J. Hodgkinson and R. P. Tatam, "Optical gas sensing: A review," Meas. Sci. Technol. **24**, 012004 (2012).

[13] T. Wang *et al.*, "Phonon-polaritonic bowtie nanoantennas: Controlling infrared thermal radiation at the nanoscale," ACS Photonics **4**, 1753–1760 (2017).

01 September 2025 00:38:52

[14]K. Sun, Y. Cai, L. Huang, and Z. Han, "Ultra-narrowband and rainbow-free mid-infrared thermal emitters enabled by a flat band design in distorted photonic lattices," Nat. Commun. **15**, 4019 (2024).

[15]J. D. Caldwell *et al.*, "Low-loss, infrared and terahertz nanophotonics using surface phonon polaritons," Nanophotonics **4**, 44–68 (2015).

[16]P. Rufangura, T. G. Folland, A. Agrawal, J. D. Caldwell, and F. Iacopi, "Towards low- loss on-chip nanophotonics with coupled graphene and silicon carbide: A review," J. Phys.: Mater. **3**, 032005 (2020).

[17]J.-J. Greffet *et al.*, "Coherent emission of light by thermal sources," Nature **416**, 61–64 (2002).

[18]C. Arnold *et al.*, "Coherent thermal infrared emission by two-dimensional silicon carbide gratings," Phys. Rev. B **86**, 035316 (2012).

[19]J. A. Schuller, T. Taubner, and M. L. Brongersma, "Optical antenna thermal emitters," Nat. Photonics **3**, 658–661 (2009).

[20]G. Lu *et al.*, "Engineering the spectral and spatial dispersion of thermal emission via polariton–phonon strong coupling," Nano Lett. **21**, 1831–1838 (2021).

[21]S. Zare *et al.*, "Probing near-field thermal emission of localized surface phonons from silicon carbide nanopillars," ACS Photonics **10**, 401–411 (2023).

[22]A. Howes, J. R. Nolen, J. D. Caldwell, and J. Valentine, "Near-unity and narrowband thermal emissivity in balanced dielectric metasurfaces," Adv. Opt. Mater. **8**, 1901470 (2020).

[23]A. Yi *et al.*, "Silicon carbide for integrated photonics," Appl. Phys. Rev. **9**, 031302 (2022).

[24]R. Soref, "Mid-infrared photonics in silicon and germanium," Nat. Photonics **4**, 495–497 (2010).

[25]A. M. Dubrovkin *et al.*, "Resonant nanostructures for highly confined and ultrasensitive surface phonon-polaritons," Nat. Commun. **11**, 1863 (2020).

[26]B. Qiang *et al.*, "Germanium-on-carborundum surface phonon-polariton infrared metamaterial," Adv. Opt. Mater. **9**, 2001652 (2021).

[27]F. Cui and G. Zheng, "Photonic-grating-enabled selective manipulation of surface waves within the reststrahlen band," Opt. Mater. **122**, 111814 (2021).

[28]B. Ma *et al.*, "Narrowband diffuse thermal emitter based on surface phonon polaritons," Nanophotonics **11**, 4115–4122 (2022).

[29]W. G. Spitzer, D. A. Kleinman, and C. J. Frosch, "Infrared properties of cubic silicon carbide films," Phys. Rev. **113**, 133 (1959).

[30]X. Qian, P. Jiang, and R. Yang, "Anisotropic thermal conductivity of 4H and 6H silicon carbide measured using time-domain thermoreflectance," Mater. Today Phys. **3**, 70–75 (2017).

[31]M. Amjadipour, J. MacLeod, N. Motta, and F. Iacopi, "Fabrication of free-standing silicon carbide on silicon microstructures via massive silicon sublimation," J. Vac. Sci. Technol., B **38**, 062202 (2020).

[32]S. A. Maier, *Plasmonics: Fundamentals and Applications* (Springer Science & Business Media, 2007).

[33]Y. Chen *et al.*, "Spectral tuning of localized surface phonon polariton resonators for low-loss mid-IR applications," ACS Photonics **1**, 718–724 (2014).

[34]Y. Yang, S. Taylor, H. Alshehri, and L. Wang, "Wavelength-selective and diffuse infrared thermal emission mediated by magnetic polaritons from silicon carbide metasurfaces," Appl. Phys. Lett. **111**, 051904 (2017).

[35]A. M. Dubrovkin, B. Qiang, H. N. S. Krishnamoorthy, N. I. Zheludev, and Q. J. Wang, "Ultra-confined surface phonon polaritons in molecular layers of van der Waals dielectrics," Nat. Commun. **9**, 1762 (2018).

[36]F. Marquier *et al.*, "Coherent spontaneous emission of light by thermal sources," Phys. Rev. B **69**, 155412 (2004).

[37]X. Wu *et al.*, "A dual-selective thermal emitter with enhanced subambient radiative cooling performance," Nat. Commun. **15**, 815 (2024).

[38]J.-S. Lim *et al.*, "Multiresonant selective emitter with enhanced thermal management for infrared camouflage," ACS Appl. Mater. Interfaces **16**, 15416–15425 (2024).

[39]J. Meng, S. Balendhran, Y. Sabri, S. K. Bhargava, and K. B. Crozier, "Smart mid-infrared metasurface microspectrometer gas sensing system," Microsyst. Nanoeng. **10**, 74 (2024).

[40]N. J. Bareza *et al.*, "Phonon-enhanced mid-infrared CO_2 gas sensing using boron nitride nanoresonators," ACS Photonics **9**, 34–42 (2022).

[41]A. Livingood *et al.*, "Filterless nondispersive infrared sensing using narrowband infrared emitting metamaterials," ACS Photonics **8**, 472–480 (2021).

[42]A. Lochbaum *et al.*, "On-chip narrowband thermal emitter for mid-IR optical gas sensing," ACS Photonics **4**, 1371–1380 (2017).

[43]X. Liu *et al.*, "Taming the blackbody with infrared metamaterials as selective thermal emitters," Phys. Rev. Lett. **107**, 045901 (2011).

[44]G. Lu *et al.*, "Collective phonon–polaritonic modes in silicon carbide subarrays," ACS Nano **16**, 963–973 (2021).

[45]S. Shin, M. Elzouka, R. Prasher, and R. Chen, "Far-field coherent thermal emission from polaritonic resonance in individual anisotropic nanoribbons," Nat. Commun. **10**, 1377 (2019).

[46]D. Chen *et al.*, "Realization of near-perfect absorption in the whole reststrahlen band of SiC," Nanoscale **10**, 9450–9454 (2018).

[47]S. Adachi, *Optical Properties of Crystalline and Amorphous Semiconductors: Materials and Fundamental Principles* (Springer Science & Business Media, 2012).

[48]P. Rufangura *et al.*, "Enhanced absorption with graphene-coated silicon carbide nanowires for mid-infrared nanophotonics," Nanomaterials **11**, 2339 (2021).

[49]M. A. Stroscio and M. Dutta, *Phonons in Nanostructures* (Cambridge University Press, 2001).

[50]T. G. Folland and J. D. Caldwell, *Advanced Study Institute on NATO ASI on Quantum Nano-Photonics* (Springer, 2017), pp. 235–254.

[51]D. P. Edward and I. Palik, *Handbook of Optical Constants of Solids* (Academic Press, Orlando, FL, 1985).

01 September 2025 00:38:52